

# Constraining dark matter halo properties using lensed Supernova Legacy Survey supernovae

J. Jönsson,<sup>1\*</sup> M. Sullivan,<sup>1</sup> I. Hook,<sup>1,2</sup> S. Basa,<sup>3</sup> R. Carlberg,<sup>4</sup> A. Conley,<sup>4</sup> D. Fouchez,<sup>5</sup> D. A. Howell,<sup>6,7</sup> K. Perrett<sup>4</sup> and C. Pritchett<sup>8</sup>

<sup>1</sup>University of Oxford Astrophysics, Denys Wilkinson Building, Keble Road, Oxford OX1 3RH

<sup>2</sup>INAF – Osservatorio Astronomico di Roma, via Frascati 33, 00040 Monteporzio (RM), Italy

<sup>3</sup>LAM, Observatoire Astronomique de Marseille, Pôle de l'Étoile Site de Château-Gombert 38, rue Frédéric Joliot–Curie 13388 Marseille cedex 13, France

<sup>4</sup>Department of Astronomy and Astrophysics, University of Toronto, Toronto, Ontario M5S 3H4, Canada

<sup>5</sup>CPPM, CNRS–IN2P3 and Université Aix–Marseille II, Case 907, 13288 Marseille Cedex 9, France

<sup>6</sup>Las Cumbres Observatory Global Telescope Network, 6740 Cortona Dr., Suite 102, Goleta, CA 93117, USA

<sup>7</sup>Department of Physics, University of California, Santa Barbara, Broida Hall, Mail Code 9530, Santa Barbara, CA 93106–9530, USA

<sup>8</sup>Department of Physics & Astronomy, University of Victoria, Victoria, BC V8W 3P6, Canada

Accepted 2010 February 2. Received 2010 February 1; in original form 2009 November 9

## ABSTRACT

This paper exploits the gravitational magnification of Type Ia supernovae (SNe Ia) to measure properties of dark matter haloes. Gravitationally magnified and de-magnified SNe Ia should be brighter and fainter than average, respectively. The magnification of individual SNe Ia can be computed using observed properties of foreground galaxies and dark matter halo models. We model the dark matter haloes of the galaxies as truncated singular isothermal spheres with velocity dispersion and truncation radius obeying luminosity-dependent scaling laws.

A homogeneously selected sample of 175 SNe Ia from the first 3 yr of the Supernova Legacy Survey (SNLS) in the redshift range  $0.2 \lesssim z \lesssim 1$  is used to constrain models of the dark matter haloes associated with foreground galaxies. The best-fitting velocity dispersion scaling law agrees well with galaxy–galaxy lensing measurements. We further find that the normalization of the velocity dispersion of passive and star-forming galaxies are consistent with empirical Faber–Jackson and Tully–Fisher relations, respectively. If we make no assumption on the normalization of these relations, we find that the data prefer gravitational lensing at the 92 per cent confidence level. Using recent models of dust extinction, we deduce that the impact of this effect on our results is very small.

We also investigate the brightness scatter of SNe Ia due to gravitational lensing, which has implications for SN Ia cosmology. The gravitational lensing scatter is approximately proportional to the SN Ia redshift. We find the constant of proportionality to be  $B \simeq 0.055^{+0.039}_{-0.041}$  mag ( $B \lesssim 0.12$  mag at the 95 per cent confidence level). If this model is correct, the contribution from lensing to the intrinsic brightness scatter of SNe Ia is small for the SNLS sample. According to the best-fitting dark matter model, gravitational lensing should, however, contribute significantly to the brightness scatter at  $z \gtrsim 1.6$ .

**Key words:** gravitational lensing – supernovae: general – galaxies: haloes – dark matter.

## 1 INTRODUCTION

In the context of supernova cosmology, gravitational lensing is usually regarded as a source of uncertainty because it adds extra scatter to the brightness of high-redshift Type Ia supernovae (SNe Ia) (Kantowski, Vaughan & Branch 1995; Frieman 1997; Wambsganss

et al. 1997; Holz & Wald 1998; Bergström et al. 2000; Holz & Linder 2005; Gunnarsson et al. 2006). Due to flux conservation, the effects of gravitational lensing magnification and de-magnification average out and are therefore expected to lead to negligible bias in cosmological parameter estimation (see e.g. Jönsson et al. 2008; Sarkar et al. 2008).

Gravitationally lensed SNe Ia are, however, interesting in their own right, because they can be used to measure magnification. Magnified and de-magnified standard candles, like SNe Ia calibrated

\*E-mail: jacke@astro.ox.ac.uk

using light-curve shape and colour corrections, should appear to be brighter and fainter than average, respectively. Cosmic magnification has already been detected by Scranton et al. (2005) using the correlation between quasars and galaxies observed within the Sloan Digital Sky Survey. The magnification (or de-magnification) of SNe Ia can be used to probe cosmology (Metcalf 1999; Dodelson & Vallinotto 2006; Zentner & Bhattacharya 2009) and the nature of the lensing matter (Rauch 1991; Metcalf 1998; Metcalf & Silk 1999; Seljak & Holz 1999; Mörtzell, Goobar & Bergström 2001; Minty, Heavens & Hawkins 2002; Metcalf & Silk 2007; Jönsson et al. 2010).

In addition to this paper, there is another lensing study making use of Supernova Legacy Survey (SNLS; Astier et al. 2006) data. The study of Kronborg et al. (2010), which focuses on the detection of a gravitational lensing signal using assumptions about the dark matter halo models, reports the detection of a signal at the 99 per cent confidence level. This result confirms an earlier tentative detection with Great Observatories Origins Deep Survey (GOODS) data (Jönsson et al. 2007). In the work presented here, the assumptions of the underlying model are tested.

We use presumably lensed high-redshift ( $0.2 \lesssim z \lesssim 1$ ) SNe Ia from the SNLS, to measure properties of dark matter haloes of galaxies in the deep Canada–France–Hawaii Telescope Legacy Survey (CFHTLS) fields. The method we use was first suggested by Metcalf (1998). Recently, Jönsson et al. (2010) applied this method to SNe Ia and galaxies observed within the GOODS. Since the SNLS SNe Ia are not as distant ( $z \lesssim 1$ ) as the GOODS SNe Ia, the effect of gravitational lensing is expected to be smaller than for the GOODS sample. However, the SNLS SNe Ia are far more numerous and selected in a more homogeneous way.

The data used to put constraints on dark matter halo properties are described in Section 2. In Section 3, the method is described. The results are presented in Section 4. We investigate the effect of dust extinction in Section 5. Section 6 is devoted to gravitational lensing brightness scatter. The results are summarized and discussed in Section 7.

Throughout the paper, we assume a cosmological model characterized by  $\Omega_M = 0.27$ ,  $\Omega_\Lambda = 0.73$  and  $h = 0.7$ .

## 2 DATA

The SNLS is made up of photometric and spectroscopic observations. The photometry is obtained as part of the deep component of CFHTLS with the  $1 \text{ deg}^2$  imager MegaCam (Boulade et al. 2003). The deep part of CFHTLS comprises four fields (D1, D2, D3 and D4), each  $\simeq 1 \text{ deg}^2$  in size, imaged in  $u^*$ ,  $g'$ ,  $r'$ ,  $i'$  and  $z'$  filters approximately every 4–5 d during dark and grey time, suitable for detecting supernovae and building light curves (Astier et al. 2006; Guy et al., in preparation). The spectroscopic observations are used to determine the nature of supernova candidates and measure their redshifts (Howell et al. 2005; Bronder et al. 2008; Balland et al. 2009). To measure properties of dark matter galaxy haloes using lensed SNe Ia, observations of both supernovae and galaxies are required.

### 2.1 Galaxies

The number of galaxies in each field is of the order  $10^5$  and we therefore have to rely upon photometric redshifts. The techniques used to obtain galaxy properties are described in detail in Sullivan et al. (2006). Galaxy photometry is performed using *SEXTRACTOR*

(Bertin & Arnouts 1996) following Sullivan et al. (2006). We estimate the galaxy redshift,  $z_{\text{gal}}$ , and its physical properties using the photometric redshift code *Z-PEG*, based on the *PÉGASE.2* galaxy spectral evolution code (Fioc & Rocca-Volmerange 1997; Le Borgne & Rocca-Volmerange 2002). The best-fitting spectral energy distribution (SED) is determined using a  $\chi^2$  minimization between the observed fluxes, the corresponding flux errors and the synthetic photometry generated by integrating the template SEDs through the SNLS effective filter responses.

We then use this best-fitting SED for the estimation of the various properties which can be used to characterize the galaxy. We first require an appropriate luminosity. The galaxies could, in principle, be characterized by the luminosity in any rest-frame wavelength band, but to facilitate comparison with results in the literature we use  $M_B$ , the absolute magnitude in the *B* band. Given the photometric redshift of a galaxy and the best-fitting SED, we compute absolute magnitudes by integrating the de-redshifted SED through the *B*-band filter.

We also require a galaxy type  $\tau$  as we expect the relations between dark matter haloes and galaxies to be different for different galaxy types. As in Sullivan et al. (2006), we use the specific star formation rate (sSFR), the star formation rate (in  $M_\odot \text{ yr}^{-1}$ ) per unit stellar mass. If  $\log(\text{sSFR}) < -12$ , the galaxy is classified as passive, otherwise it is classified as star forming.

According to Ilbert et al. (2006), reliable photometric redshifts can only be obtained for galaxies with  $m_{i'} < 24 \text{ mag}$  from the CFHTLS deep data. We therefore include only galaxies brighter than this magnitude limit. The fraction of passive galaxies ranges from 5 per cent in D1 and D3 to 8 per cent in D4. We have checked that including galaxies fainter than  $m_{i'} = 24 \text{ mag}$ , which have less secure redshifts, have negligible impact on the results.

### 2.2 Supernovae

We assume that the brightness of an SN Ia traces its magnification. In our analysis, we use the Hubble diagram residual,

$$\Delta m_{\text{SN}} = \mu_B - \mu(\Omega_M, \Omega_\Lambda; z_{\text{SN}}), \quad (1)$$

and its uncertainty,  $\sigma_{\Delta m_{\text{SN}}}$ , to characterize the brightness of an SN Ia. In the equation above,  $\mu_B$  is a distance indicator and  $\mu(\Omega_M, \Omega_\Lambda; z_{\text{SN}})$  is the predicted value for an SN Ia at redshift  $z_{\text{SN}}$  assuming a cosmological model with  $\Omega_M = 0.27$  and  $\Omega_\Lambda = 0.73$ . The Hubble diagram residual measures the brightness of an individual SN relative to the average of the population – brighter SNe have more negative residuals.

Our set of residuals was computed using the *SIFTO* (Conley et al. 2008) light-curve fitting package. We have also performed the analysis with residuals computed using the *SALT2* (Guy et al. 2007) package. The results obtained using *SIFTO* and *SALT2* residuals are very similar and we therefore only present results obtained using *SIFTO* residuals here. For this set of residuals, the intrinsic scatter, i.e. the component of the scatter which cannot be attributed to known observational errors, is approximately 0.09 mag (Guy et al., in preparation).

In order to compute the magnification due to the galaxies in the foreground, we also need, in addition to the redshift,  $z_{\text{SN}}$ , the position on the sky,  $\theta_{\text{SN}}$ , for each SN Ia. When available, we use the spectroscopic redshift of the host galaxy, otherwise the spectroscopic redshift of the SN Ia itself. Positions of the SNe Ia, as well as of the galaxies, were obtained from the CFHTLS  $i'$ -band photometry.

**Table 1.** Number of SNe Ia in the CFHTLS deep fields.

Field	All SNe Ia	Selected SNe Ia
D1	55	42
D2	49	33
D3	75	55
D4	64	45
Total	243	175

We use 243 SNe Ia from the 3-yr SNLS data set (Guy et al., in preparation). Since some parts of the deep CFHTLS fields are covered by bright stars, they have to be masked (Sullivan et al. 2006). SNe Ia located too close to a masked region or the boundary of the field are removed from the sample because of the lack of observations of foreground galaxies. To characterize the size of a masked region, we use an effective radius,  $\theta_{\text{eff}} = \sqrt{A/\pi}$ , where  $A$  is the area of the masked region. The effective radius ranges from a few to a few hundred arcsec. Roughly 20 per cent of the deep fields are covered by masked regions, but most of this area is made up of a few regions with  $\theta_{\text{eff}} > 60$  arcsec.

When computing the magnification, all galaxies within a radius  $\theta_c$  are included. We use  $\theta_c = 60$  arcsec, which according to simulations (Gunnarsson et al. 2006; Kronborg et al. 2010) is sufficient. For an SN Ia to be included in the analysis, we therefore use the selection criterion that the distance to the boundary of the field or the distance to the boundary of the nearest masked region must be larger than  $\theta_c$ . If all masked regions were taken into account, most SNe Ia would lie too close to a masked region and for that reason fail the selection criterion. We therefore ignore all masked regions with  $\theta_{\text{eff}} < 20$  arcsec. Since the location of the masked regions should be uncorrelated with the location of the foreground galaxies, ignoring small masked regions should not bias the results, only increase the uncertainty.

Only 175 out of the 243 SNe Ia fulfil the selection criterion. In Table 1, the total number of SNe Ia together with the number of selected ones are listed for each field.

### 3 METHOD

The method (Metcalf 1998) we use can be summarized in two steps. First, the magnifications of the SNe Ia are computed for a range of halo models. Then, the best-fitting halo model to the Hubble diagram residuals is obtained by  $\chi^2$  minimization. In the following, the method is described in more detail.

#### 3.1 Computing the magnification

In order to constrain properties of dark matter haloes, we exploit the correlation between the brightness of SNe Ia and their magnification. For each SN Ia, the gravitational magnification due to the dark matter haloes associated with the observed galaxies in the foreground,  $\Delta m_{\text{lens}}(\lambda_{\text{SN}}, \lambda_{\text{los}}; \lambda_{\text{halo}})$ , is computed assuming a halo model with parameters described by  $\lambda_{\text{halo}}$ . To describe the redshift,  $z_{\text{SN}}$ , and location,  $\theta_{\text{SN}}$ , of the SN Ia, which are used in the calculation, we use the shorthand notation

$$\lambda_{\text{SN}} = \{z_{\text{SN}}, \theta_{\text{SN}}\}. \quad (2)$$

For the calculation of the magnification, we also need properties of the  $N_{\text{gal}}$  galaxies along the SN Ia line of sight, which we denote by

$$\lambda_{\text{los}} = \left\{ z_{\text{gal}}^1, \theta_{\text{gal}}^1, M_B^1, \tau^1, \dots, z_{\text{gal}}^{N_{\text{gal}}}, \theta_{\text{gal}}^{N_{\text{gal}}}, M_B^{N_{\text{gal}}}, \tau^{N_{\text{gal}}} \right\}, \quad (3)$$

where  $z_{\text{gal}}^i$ ,  $\theta_{\text{gal}}^i$ ,  $M_B^i$  and  $\tau^i$  are redshift, position on the sky, absolute  $B$ -band magnitude and type of the  $i$ th galaxy.

To compute the magnification of an SN Ia, we use the weak lensing approximation (see, for example, Schneider, Ehlers & Falco 1992). We have checked the validity of this approximation against a more time-consuming ray-tracing algorithm for a few cases. For the sample of SNe Ia considered here, which have relatively low redshifts, the difference is found to be  $\lesssim 5$  per cent.

According to the weak lensing approximation, the magnification, in terms of magnitudes, is related to the convergence,  $\kappa$ , (which is a dimensionless surface density) via

$$\Delta m_{\text{lens}} \simeq -2.17\kappa, \quad (4)$$

where

$$\kappa = \kappa_{\text{los}} - \kappa_{\text{b}}. \quad (5)$$

The first term in equation (5) is a sum over the contribution to the convergence from each galaxy,  $\kappa_{\text{gal}}$ , along the line of sight,

$$\kappa_{\text{los}} = \sum_{i=1}^{N_{\text{gal}}} \kappa_{\text{gal}}^i. \quad (6)$$

The second term, representing the compensating effect of the background density, acts as a normalization allowing the magnification relative to a homogeneous universe to be computed. Due to flux conservation,  $\langle \kappa \rangle = 0$ . To ensure that this condition is fulfilled, we use  $\kappa_{\text{b}} = \langle \kappa_{\text{los}} \rangle$ . The average value of  $\kappa_{\text{los}}$  is computed for a large number of randomly selected lines of sight. One important element of the model remains to specify, namely  $\kappa_{\text{gal}}$ .

#### 3.2 Halo models

The contribution to the dimensionless convergence from each galaxy is given by

$$\kappa_{\text{gal}}(\xi) = \frac{\Sigma(\xi)}{\Sigma_c}, \quad (7)$$

where the surface density,  $\Sigma(\xi)$ , is obtained by projecting the matter distribution on to a lens plane,

$$\Sigma(\xi) = \int_{-\infty}^{\infty} \rho(\xi, y) dy, \quad (8)$$

where  $\xi$  is a vector in the plane and  $y$  is a coordinate along the line of sight. This is the step in the calculations where the density profile,  $\rho(\mathbf{r})$ , of the dark matter halo enters. Equation (7) depends also on the critical surface density,

$$\Sigma_c = \frac{1}{4\pi G} \frac{D_s}{D_d D_{\text{ds}}}, \quad (9)$$

which, in turn, depends on the angular diameter distances between the observer and the source,  $D_s$ , the observer and the lens (deflector),  $D_d$ , and the lens and the source,  $D_{\text{ds}}$ . The distances are computed from  $z_{\text{SN}}$  and  $z_{\text{gal}}$  assuming a cosmological model ( $\Omega_{\text{M}} = 0.27$ ,  $\Omega_{\Lambda} = 0.73$  and  $h = 0.7$ ).

We assume that the dark matter haloes can be described by a singular isothermal sphere (SIS). The density profile of an SIS,

$$\rho(r) = \frac{\sigma^2}{2\pi G} \frac{1}{r^2}, \quad (10)$$

has only one free parameter – the velocity dispersion,  $\sigma$ . The formula for the convergence of an SIS can be considerably simplified, if we introduce a suitable length-scale  $\xi_0$  in the lens plane,

$$\xi_0 = 4\pi\sigma^2 \frac{D_d D_{\text{ds}}}{D_s}. \quad (11)$$

Since the SIS profile is divergent, the profile is truncated at a radius  $r_t$ . The convergence of a truncated SIS is given by

$$\kappa_{\text{gal}}(x) = \begin{cases} \frac{1}{\pi x} \arctan \sqrt{x_t^2/x^2 - 1} & \text{if } x \leq x_t \\ 0 & \text{if } x > x_t, \end{cases} \quad (12)$$

where  $x = \xi/\xi_0$  and  $x_t = r_t/\xi_0$ .

To investigate the relationship between galaxy luminosity and velocity dispersion, we use the scaling law

$$\sigma = \sigma_* \left( \frac{L}{L_*} \right)^\eta, \quad (13)$$

where  $L_*$  is a fiducial luminosity, which we take to be  $L_* = 10^{10} h^{-2} L_\odot$  in the  $B$  band. In terms of absolute  $B$ -band magnitudes, which we will work with, the scaling relation becomes

$$\sigma = \sigma_* 10^{-\eta(M_B - M_B^*)/2.5}, \quad (14)$$

where  $M_B^* = -19.52 + 5 \log_{10} h$ .

For the truncation radius, we will consider a scaling law of the form

$$r_t = r_* \left( \frac{\sigma}{\sigma_*} \right)^\gamma = r_* \left( \frac{L}{L_*} \right)^{\eta\gamma}. \quad (15)$$

Since we only include galaxies located at distance  $\theta_c$  from the position of the SN Ia, the truncation radius has an effect only if  $r_t/D_d < \theta_c$ . For  $\theta_c = 60 \text{ arcsec}$  and  $z_{\text{gal}} < 1$ , this corresponds to  $r_t \lesssim 300 h^{-1} \text{ kpc}$ .

### 3.3 Finding the best-fitting model

In summary, the parameters of our halo model are

$$\lambda_{\text{halo}} = \{\sigma_*, \eta, r_*, \gamma\}, \quad (16)$$

where  $\{\sigma_*, \eta\}$  and  $\{r_*, \gamma\}$  describe the velocity dispersion and truncation radius scaling law, respectively.

To find the best-fitting halo model, we minimize the following  $\chi^2$ -function:

$$\chi^2 = \sum_{i=1}^{N_{\text{SN}}} \frac{[\Delta m_{\text{SN}}^i - \Delta m_{\text{lens}}(\lambda_{\text{SN}}^i, \lambda_{\text{los}}^i; \lambda_{\text{halo}})]^2}{\sigma_{\text{int}}^2 + (\sigma_{\Delta m_{\text{SN}}}^i)^2}, \quad (17)$$

where the superscript  $i$  refers to the  $i$ th SN Ia.

In equation (17), the intrinsic dispersion,  $\sigma_{\text{int}}$ , is added in quadrature to the uncertainty of the Hubble diagram residual. The uncertainty in  $\Delta m_{\text{lens}}(\lambda_{\text{SN}}, \lambda_{\text{los}}; \lambda_{\text{halo}})$ , which for a specific halo model  $\lambda_{\text{halo}}$  only depends on the uncertainties in  $\lambda_{\text{SN}}$  and  $\lambda_{\text{los}}$ , is negligible compared to  $\sigma_{\text{int}}$  and  $\sigma_{\Delta m_{\text{SN}}}$  and is for that reason neglected in equation (17).

### 3.4 Cosmic variance

The four deep CFHTLS fields are located widely separated in the sky. Due to cosmic variance, we expect the density of galaxies to vary between the fields. This variation affects the normalization of the convergence,  $\kappa_b$ . Fig. 1 shows  $\kappa_b$  as a function of source redshift for the four fields computed for two different SIS models. For both models,  $\eta = 1/3$  and  $\gamma = 0$ . The lower set of curves correspond to  $\sigma_* = 130 \text{ km s}^{-1}$  and  $r_* = 40 h^{-1} \text{ kpc}$ , while the upper set of curves corresponds to  $\sigma_* = 130 \text{ km s}^{-1}$  and  $r_* = 200 h^{-1} \text{ kpc}$ . For both models, the differences between the fields increase with source redshift. In order to reduce the effect of cosmic variance, we use the average value of  $\kappa_b$ , as indicated by the circles.

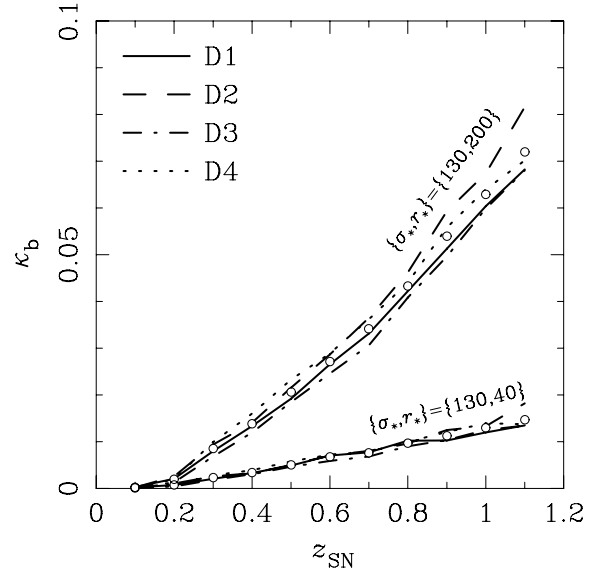


**Figure 1.** Convergence normalization,  $\kappa_b$ , as a function of source redshift. Solid, dashed, dash-dotted and dotted curves correspond to D1, D2, D3 and D4, respectively. The two sets of curves are computed for two different SIS models. For both models,  $\eta = 1/3$  and  $\gamma = 0$ , but the values of  $\sigma_*$  (measured in  $\text{km s}^{-1}$ ) and  $r_*$  (measured in  $h^{-1} \text{ kpc}$ ) differ. The lower and upper set of curves correspond to  $\{\sigma_*, r_*\} = \{130, 200\}$  and  $\{\sigma_*, r_*\} = \{130, 40\}$ , respectively. Open circles indicate the average of  $\kappa_b$  computed for the four fields.

## 4 RESULTS

The halo model,  $\lambda_{\text{halo}}$ , has four parameters. Instead of constraining all parameters simultaneously, which would be quite time consuming, we focus on different aspects of the model in the following.

### 4.1 Truncation radius

Our model of the luminosity-dependent truncation radius, equation (15), has two parameters:  $r_*$  and  $\gamma$ . In order to reduce the size of the parameter space to a manageable size, the investigation is limited to a single value of  $\eta$  in equation (13). We expect this parameter to be in the range  $1/4 \lesssim \eta \lesssim 1/3$ , since  $\eta \simeq 1/4$  and  $\eta \simeq 1/3$  are the exponents belonging to the Faber–Jackson (F–J; Faber & Jackson 1976) and Tully–Fisher (T–F; Tully & Fisher 1977) relations valid for early- and late-type galaxies, respectively. Since most of the galaxies in our sample are star forming and therefore should be of late type, we assume  $\eta = 1/3$ . We have checked that the dependence of  $\eta$  is rather weak, justifying our restricted investigation.

When minimizing equation (17) with respect to the three parameters, we find two minima with similar  $\chi^2$ . For the first minimum ( $\sigma = 114 \text{ km s}^{-1}$ ,  $r_* = 170 h^{-1} \text{ kpc}$ ,  $\gamma = -2.8$ ), the value of the  $\chi^2$  is 164.50. The  $\chi^2$  for the second minimum ( $\sigma = 124 \text{ km s}^{-1}$ ,  $r_* = 69 h^{-1} \text{ kpc}$ ,  $\gamma = -0.9$ ) is slightly higher, 164.66. The best-fitting velocity dispersion normalizations,  $\sigma_*$ , are similar for the two minima. Negative values of  $\gamma$  correspond to rather peculiar truncation radius scaling laws. For these scaling laws, more luminous, and presumably more massive, galaxies have smaller truncation radii than less luminous galaxies. Unfortunately, the data do not allow us to put any limits on  $r_*$  and  $\gamma$ .

Fortunately, limits can be obtained for the normalization of the velocity dispersion. Fig. 2 shows the probability density function of  $\sigma_*$  after marginalization over  $r_*$  and  $\gamma$ . We find  $\sigma_* = 83^{+37}_{-56} \text{ km s}^{-1}$

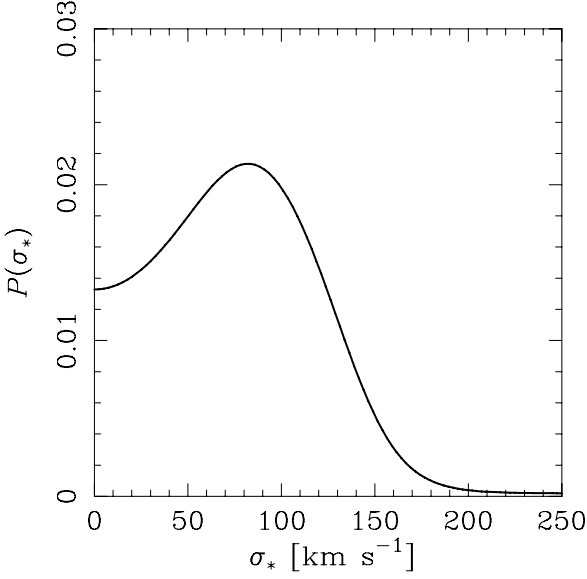


**Figure 2.** Probability density function of  $\sigma_*$  after marginalization over  $r_*$  and  $\gamma$ . The exponent of the luminosity-dependent velocity dispersion scaling law is  $\eta = 1/3$ .

(68.3 per cent confidence level) and  $\sigma_* < 147 \text{ km s}^{-1}$  at 95 per cent confidence level.

Let us now compare the best-fitting values of the truncation radius with the virial radius. The virial radius is defined as the radius inside which the mean density of the halo is  $\Delta_{\text{vir}}(z)$  times the mean matter density,  $\rho_m(z) = \Omega_M \rho_c^0 (1+z)^3$ , where  $\rho_c^0$  is the present critical density. To compute the virial over density, we use the approximation of Bryan & Norman (1998),

$$\Delta_{\text{vir}}(z) \simeq (18\pi^2 + 82x - 39x^2)\rho_c(z)/\rho_m(z), \quad (18)$$

where  $x = \rho_m(z)/\rho_c(z) - 1$ . For an SIS profile, the virial radius is

$$r_{\text{vir}} = 20\sigma \left[ \Delta_{\text{vir}}(z)\Omega_M(1+z)^3 \right]^{-1/2} h^{-1} \text{ kpc}. \quad (19)$$

From equations (7) and (9), it is clear that there is an optimum lens redshift,  $z_{\text{gal}}$ , for every source redshift,  $z_{\text{SN}}$ , depending on the distance combination  $D_d D_{\text{ds}}/D_s$ , where the convergence is maximal. Our distribution of sources peaks at  $z_{\text{SN}} \simeq 0.7$ , which corresponds to an optimum lens redshift of  $z_{\text{gal}} \simeq 0.3$ . For a dark matter halo at this redshift, the virial radius is, according to equation (19),  $r_{\text{vir}} \simeq 1.6\sigma h^{-1} \text{ kpc}$ .

The virial radius of an  $L_*$  galaxy, for which we find  $\sigma_* \simeq 120 \text{ km s}^{-1}$ , is hence  $r_{\text{vir}}^* \simeq 190 h^{-1} \text{ kpc}$ . When exploring the truncation radius scaling law, we find  $r_* = 170 h^{-1} \text{ kpc}$ , which is similar to the virial radius, but the exponent is peculiar,  $\gamma = -2.8$ . As we will see in the next section, we find even smaller values of  $r_*$  for  $\gamma = 0$ .

#### 4.2 Velocity dispersion scaling law

Let us now investigate the velocity dispersion scaling law, which is described by the parameters  $\sigma_*$  and  $\eta$ . Here, we consider a constant truncation radius,  $r_t = r_*$ , i.e. we assume  $\gamma = 0$ . The best-fitting values of the three parameters to the data are  $\sigma_* = 122 \text{ km s}^{-1}$ ,  $\eta = 0.45$  and  $r_* = 40 h^{-1} \text{ kpc}$ . This value of  $r_*$  is only one-fifth of the virial radius corresponding to  $\sigma_*$ . For this minimum, the  $\chi^2$  is 164.30. In order to obtain constraints on the velocity dispersion scaling law ( $\sigma_*$  and  $\eta$ ), we marginalize over  $r_*$ . Reasonable fits to

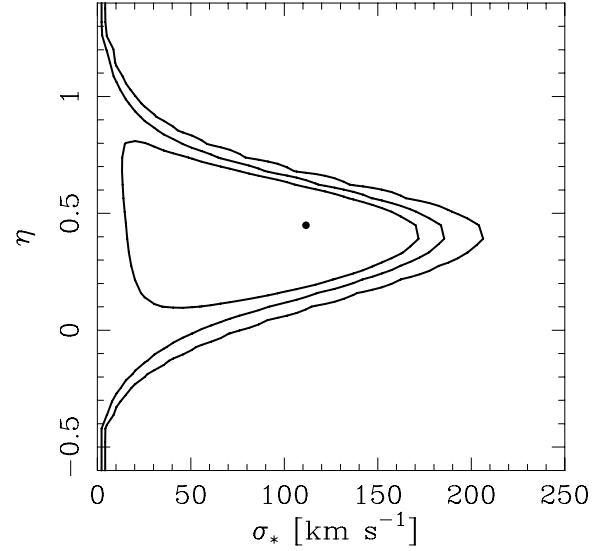


**Figure 3.** Best-fitting values (circle) and 68.3, 95 and 99 per cent confidence level contours for the luminosity-dependent velocity dispersion scaling law after marginalization over  $r_*$ .

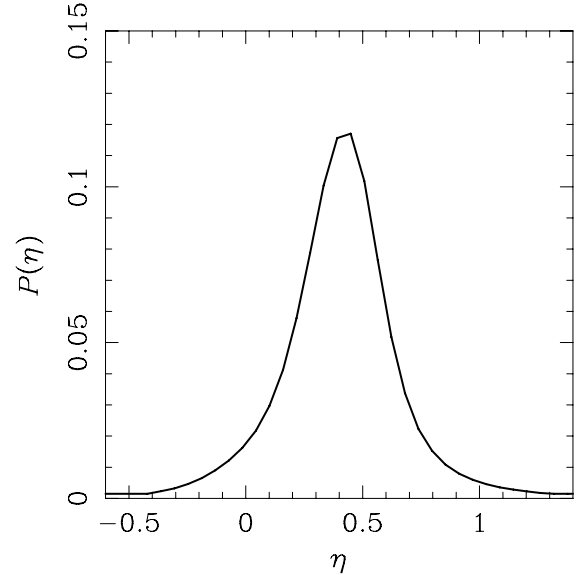


**Figure 4.** Probability density function of  $\eta$  after marginalization over  $\sigma_*$  and  $r_*$ .

the data cannot be obtained for all values of  $r_*$  and we therefore apply a flat prior,

$$\pi(r_*) = \begin{cases} 1 & \text{if } 20 h^{-1} < r_* < 100 h^{-1} \\ 0 & \text{otherwise,} \end{cases} \quad (20)$$

when marginalizing over this parameter. Fig. 3 shows the results for the velocity dispersion scaling law. The circle indicates the best-fitting values ( $\sigma_* = 112 \text{ km s}^{-1}$  and  $\eta = 0.45$ ). In the figure are also shown confidence level contours at the 68.3, 95 and 99 per cent confidence level.

Fig. 4 shows the probability density function of  $\eta$  after marginalization over  $\sigma_*$  and  $r_*$ . We find  $\eta = 0.45^{+0.19}_{-0.27}$  (68.3 per cent confidence level) and  $-0.34 < \eta < 1.17$  at the 95 per cent confidence level. For the velocity dispersion normalization, we can only obtain

upper limits. After marginalization over  $\eta$  and  $r_*, we find  $\sigma_* < 156$  at the 95 per cent confidence level.$

We have redone the fit of the velocity dispersion scaling law assuming the truncation radius to be equal to the virial radius, given by equation (19). The best-fitting model ( $\chi^2 = 168.13$ ) is in this case  $\sigma_* = 56 \text{ km s}^{-1}$  and  $\eta = 0.25$ . After marginalization, we find  $\sigma_* < 91 \text{ km s}^{-1}$  at the 95 per cent confidence level and  $\eta = 0.25^{+0.24}_{-0.29}$  ( $-0.27 < \eta < 1.24$  at the 95 per cent confidence level).

### 4.3 Disentangling the velocity dispersion of different galaxy types

As already noted, we expect different scaling laws for different galaxy types. The galaxies in our sample are classified as either passive or star forming depending on their sSFR (see Section 2.1). We will associate passive and star-forming galaxies with early- and late-type galaxies, respectively. For passive and star-forming galaxies, we assume the velocity dispersion to scale with luminosity as

$$\sigma^p = \sigma_*^p \left( \frac{L}{L_*} \right)^{1/4} \quad (21)$$

and

$$\sigma^{\text{sf}} = \sigma_*^{\text{sf}} \left( \frac{L}{L_*} \right)^{1/3}, \quad (22)$$

respectively. The exponents of these scaling laws correspond to the F–J and T–F relations. Once again we restrict our study to models with  $\gamma = 0$ .

For the best-fitting halo model,  $\sigma_*^p = 196 \text{ km s}^{-1}$ ,  $\sigma_*^{\text{sf}} = 109 \text{ km s}^{-1}$  and  $r_* = 45 h^{-1} \text{ kpc}$ , the  $\chi^2$  is 164.59. Fig. 5 shows a magnification–residual diagram computed for this model. We expect the points to scatter around the solid line with slope unity. The scatter around this line is  $r_{\text{corr}} = 0.22$ . For the Hubble diagram residuals, the scatter is 0.150 mag. Correcting this sample of SNe Ia for lensing (Gunnarsson et al. 2006; Jönsson, Mörtzell & Sollerman 2009)

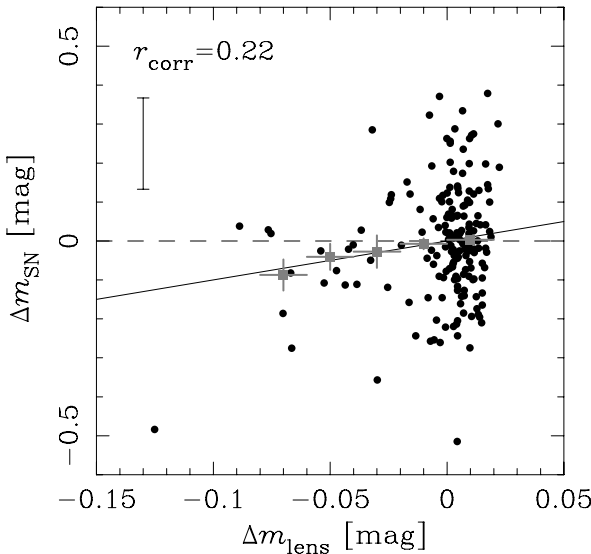


**Figure 5.** Magnification–residual diagram for the best-fitting halo model with different scaling laws for passive and star-forming galaxies. Solid squares represent the weighted average residual computed for SNe Ia in magnification bins of width 0.02 mag. An average residual error bar is shown in the upper left corner. The slope of the solid line is unity.

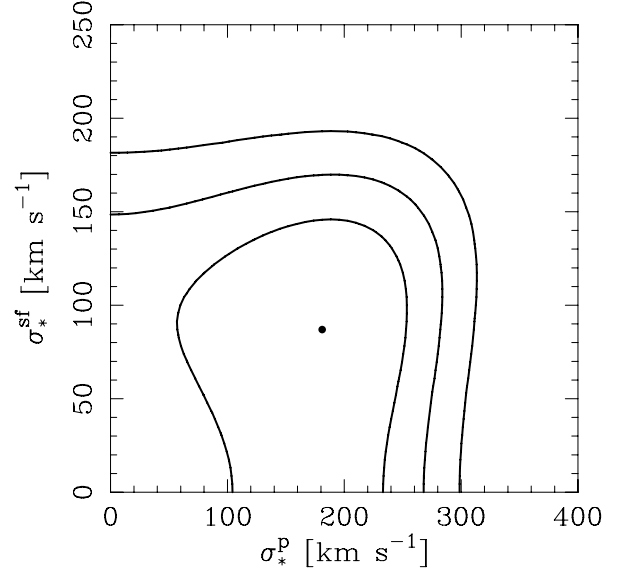


**Figure 6.** Best-fitting values (circle) and 68.3, 95 and 99 per cent confidence level contours for the velocity dispersion normalization for passive ( $\sigma_*^p$ ) and star-forming ( $\sigma_*^{\text{sf}}$ ) galaxies after marginalization over  $r_*$ .

using the best-fitting model would hence lead to a very small reduction of the scatter.

We marginalize over  $r_*$  using the prior  $\pi(r_*)$  to find constraints on  $\sigma_*^p$  and  $\sigma_*^{\text{sf}}$ . Fig. 6 shows the result of our effort to disentangle the velocity dispersion for different galaxy types. The best-fitting values ( $\sigma_*^p = 181$  and  $\sigma_*^{\text{sf}} = 87 \text{ km s}^{-1}$ ) after marginalization over  $r_*$  are indicated by the circle. The point  $\sigma_*^p = \sigma_*^{\text{sf}} = 0$ , corresponding to no lensing, is excluded at the 91.6 per cent confidence level. This detection is in good agreement with the results of Jönsson et al. (2008), where the probability of detecting lensing at this confidence level for a sample of 175 SNLS SNe Ia was predicted to be 80–90 per cent.

From Fig. 6, it is clear that larger values of the velocity dispersion are admitted for passive than for star-forming galaxies.

If we marginalize over  $r_*$  and  $\sigma_*^{\text{sf}}$  ( $\sigma_*^p$ ), we can obtain limits on  $\sigma_*^p$  ( $\sigma_*^{\text{sf}}$ ). We find  $\sigma_*^p = 181^{+60}_{-86}$  ( $\sigma_*^{\text{sf}} = 91^{+36}_{-63}$ )  $\text{km s}^{-1}$  (68.3 per cent confidence level) and  $\sigma_*^p < 260$  ( $\sigma_*^{\text{sf}} < 155$ )  $\text{km s}^{-1}$  at the 95 per cent confidence level.

When assuming  $r_t = r_{\text{vir}}$ , we find the best-fitting velocity dispersion normalization for passive and star-forming galaxies ( $\chi^2 = 167.49$ ) to be  $\sigma_*^p = 113$  and  $\sigma_*^{\text{sf}} = 33 \text{ km s}^{-1}$ , respectively. After marginalization, we find  $\sigma_*^p = 109^{+42}_{-70} \text{ km s}^{-1}$  ( $\sigma_*^p < 172 \text{ km s}^{-1}$  at the 95 per cent confidence level) for passive galaxies. For star-forming galaxies, we obtain an upper limit at the 95 per cent confidence level after marginalization,  $\sigma_*^{\text{sf}} < 101 \text{ km s}^{-1}$ . Evidently, the increased truncation radius results in lower values of the velocity dispersion normalizations. At the 99 per cent confidence level, we find  $\sigma_*^p < 195$  and  $\sigma_*^{\text{sf}} < 117 \text{ km s}^{-1}$ .

The results obtained in this section are summarized in Tables 2 and 3.

## 5 EXTINCTION BY DUST

The brightness of SNe Ia can be affected by dust extinction in addition to gravitational lensing. Extinction by dust, in contrast to gravitational lensing, leads only to dimming of SNe Ia. Extinction could therefore lead to underestimation of the effect of gravitational lensing magnification.

**Table 2.** Summary of best-fitting models.

Studied aspect of the model	Velocity dispersion scaling law		Truncation radius scaling law		$\chi^2$
	$\eta$	$\sigma_*$ (km s <sup>-1</sup> )	$\gamma$	$r_*$ (h <sup>-1</sup> kpc)	
No lensing	$\sigma = 0$				168.66
Truncation radius scaling law (first minimum)	0.33 (fixed)	114	-2.8	170	164.50
Truncation radius scaling law (second minimum)	0.33 (fixed)	124	-0.9	69	164.66
Velocity dispersion scaling law	0.45	122	0 (fixed)	40	164.30
Velocity dispersion scaling law	0.25	56	$r_t = r_{\text{vir}}$		168.13
Star-forming/passive velocity dispersion scaling law	0.33/0.25 (fixed)	109/196	0 (fixed)	45	164.59
Star-forming/passive velocity dispersion scaling law	0.33/0.25 (fixed)	33/113	$r_t = r_{\text{vir}}$		167.49

**Table 3.** Summary of constraints (with confidence level within parenthesis) on velocity dispersion scaling laws after marginalization.

Studied aspect of the model	Velocity dispersion scaling law	
	$\eta$	$\sigma_*$ (km s <sup>-1</sup> )
Truncation radius scaling law	0.33 (fixed)	$83^{+37}_{-56}$ (68.3 p.c.)
Velocity dispersion scaling law ( $\gamma = 0$ )	$0.45^{+0.19}_{-0.27}$ (68.3 p.c.)	<156 (95 p.c.)
Velocity dispersion scaling law ( $r_t = r_{\text{vir}}$ )	$0.25^{+0.24}_{-0.29}$ (68.3 p.c.)	<91 (95 p.c.)
Star-forming velocity dispersion scaling law ( $\gamma = 0$ )	0.33 (fixed)	$91^{+36}_{-63}$ (68.3 p.c.)
Passive velocity dispersion scaling law ( $\gamma = 0$ )	0.25 (fixed)	$181^{+60}_{-86}$ (68.3 p.c.)
Star-forming velocity dispersion scaling law ( $r_t = r_{\text{vir}}$ )	0.33 (fixed)	<101 (95 p.c.)
Passive velocity dispersion scaling law ( $r_t = r_{\text{vir}}$ )	0.25 (fixed)	$109^{+42}_{-70}$ (68.3 p.c.)

**Table 4.** Differences in cosmological parameters due to dust extinction correction compared to the uncorrected case.

Extinction correction	$\Delta\alpha$	$\Delta\beta$	$\Delta\mathcal{M}$	$\Delta\Omega_M$
Redshift-dependent	0.002 (0.03 $\sigma$ )	0.003 (0.03 $\sigma$ )	0.001 (0.08 $\sigma$ )	0.009 (0.50 $\sigma$ )
From individual galaxies	0.003 (0.04 $\sigma$ )	0.026 (0.26 $\sigma$ )	-0.001 (0.08 $\sigma$ )	0.007 (0.39 $\sigma$ )

Recently, Ménard et al. (2009a) used the correlation between the brightness of tens of thousands of quasars and the position of tens of millions of galaxies in the foreground to measure magnification and extinction simultaneously. According to their measurements, the average extinction and magnification have the same dependence on the impact parameter ( $\propto \xi^{-0.8}$ ).

Dust extinction and gravitational lensing can be separated because the former effect is wavelength-dependent while the latter is achromatic. In order to calibrate the SNe Ia to become standard candles, the  $B$ -band magnitude,  $m_B$ , is corrected (Astier et al. 2006),

$$\mu_B = m_B - \mathcal{M} + \alpha(s_B - 1) - \beta C, \quad (23)$$

using stretch,  $s_B$ , which parametrizes light-curve shape and colour,  $C$ . The parameters  $\mathcal{M}$ ,  $\alpha$  and  $\beta$  are determined from the data. The colour correction could potentially correct for some of the dust extinction. According to Ménard, Kilbinger & Scranton (2009b), who have investigated the consequences of dust extinction for SN Ia cosmology, this colour correction is not sufficient.

The values of the truncation radius preferred by the data are smaller than the virial radius (see Section 4). This rather surprising result might be explained by dust extinction not accounted for by the colour correction in equation (23). Another indication of the small values of  $r_t$  preferred by the data is the small values of  $\sigma_*^p$  and  $\sigma_*^{\text{sf}}$  obtained when assuming  $r_t = r_{\text{vir}}$  (see the end of Section 4.3).

We have investigated if extinction by dust could explain the small values of these halo parameters.

First, we use the high  $A_B$  model in Ménard et al. (2009b), which only depends on  $z_{\text{SN}}$  (see their fig. 1), to estimate the extinction in the  $B$  band,  $A_B$ , for each SNe Ia. The values of  $A_B$  are then used to correct  $m_B$  and  $C$  [this variable is essentially  $E(B - V)$ ] assuming a standard dust law. For the high  $A_B$  model,  $R_B = R_V + 1 = 4.9$ . Thereafter, we fit  $\Omega_M$ ,  $\mathcal{M}$ ,  $\alpha$  and  $\beta$  to the extinction-corrected data and compute new extinction-corrected residuals. These parameters are hence allowed to compensate for the effect of dust extinction. A flat universe is assumed, i.e.  $\Omega_\Lambda = 1 - \Omega_M$ . In Table 4, the differences in these parameters with respect to the uncorrected case are listed. Correcting the SNe Ia for redshift-dependent extinction has clearly a very small effect on the parameters, and consequently on the residuals. Ménard et al. (2009b) also find small differences in  $\mathcal{M}$ ,  $\alpha$  and  $\beta$  (see their table 1). For  $\Omega_M$ , however, we find only half of their difference ( $\Delta\Omega_M = 0.017$ ). The statistical significance of the difference is, however, very similar: they find  $0.55\sigma$ , whereas we find  $0.50\sigma$ . Note that the parameter  $\beta \simeq 3$  (Tripp 1998) is different from  $R_B = 4.1$  measured for Milky Way dust (Savage & Mathis 1979; Seaton 1979; Rieke & Lebofsky 1985; Cardelli, Clayton & Mathis 1989).

Finally, we redo the fit of the halo parameters  $\sigma_*^p$  and  $\sigma_*^{\text{sf}}$  using the extinction-corrected residuals. We find the difference in the best-fitting values of the halo parameters due to the extinction correction

to be negligible. This is not very surprising because the difference between the extinction-corrected and -uncorrected residuals is on average only  $0.000 \pm 0.005$  mag.

Since we have information about the foreground galaxies, the effect of a more detailed extinction correction, where the contribution from each individual galaxy is added to the total extinction, can be studied. According to the measurements of Ménard et al. (2009a), the mean extinction profile around the galaxies in their sample, which spans the brightness range  $17 < m_i < 21$ , follows

$$\langle A_V \rangle(\xi) = 4.14 \times 10^{-3} \left( \frac{\xi}{100 h^{-1} \text{ kpc}} \right)^{-0.84}. \quad (24)$$

The extinction in the  $B$  band can be obtained from the  $V$ -band extinction via  $A_B = (R_B/R_V)A_V$ . We assume the value  $R_V = 3.1$  corresponding to Milky Way dust. For our sample of SNe Ia, the more detailed model predicts larger extinctions ( $\langle A_B \rangle = 0.05$  mag) than the redshift-dependent model ( $\langle A_B \rangle = 0.03$  mag). Also for this model the differences in  $\Omega_M$ ,  $\mathcal{M}$ ,  $\alpha$  and  $\beta$  are small compared to the uncorrected case (see Table 4). For the residuals, the mean difference is  $0.000 \pm 0.009$  mag. The value of  $\beta$  is, however, slightly larger than for the redshift-dependent extinction model. The halo parameters  $\sigma_*^p$  and  $\sigma_*^{\text{sf}}$  are slightly increased by  $10 \text{ km s}^{-1}$  each, when the extinction-corrected residuals are used in the fitting procedure.

Consequently, neither of the two dust extinction models have a significant impact on the results. We conclude therefore that dust extinction is not a plausible explain for the small values of the velocity dispersion normalizations we find for  $r_t = r_{\text{vir}}$ .

## 6 GRAVITATIONAL LENSING BRIGHTNESS SCATTER

The results of the previous sections allow us to investigate the implications for supernova cosmology. We restrict ourselves to the model investigated in Section 4.3, where passive and star-forming galaxies are described by different velocity dispersion scaling laws. This model is more realistic than the ones where all galaxies are treated as if they were of the same type.

As already stated in the introduction, gravitational magnification leads to additional SN Ia brightness scatter. This scatter is expected to increase with redshift. The thick solid curve in Fig. 7 indicates the dispersion in  $\Delta m_{\text{lens}}$  as a function of redshift computed for the best-fitting model after marginalization over  $r_*$  using randomly selected lines of sight. We use the best-fitting truncation radius,  $r_* = 45 h^{-1} \text{ kpc}$ . The light and dark shaded regions indicate the scatter at the 68.3 and 95 per cent confidence level translated from Fig. 6.

Using simulations, Holz & Linder (2005) predicted the increase in lensing dispersion to be approximately proportional to the SN Ia redshift,  $\sigma_{\Delta m_{\text{lens}}} = B z_{\text{SN}}$ , with  $B = 0.088$  mag. In Fig. 7, we show the predicted dispersion for constants of proportionality in the range  $B = 0.01, 0.02, \dots, 0.15$  mag. From the figure, we conclude that it is reasonable to describe the redshift dependence of the lensing scatter as proportional to the SN Ia redshift. Other authors have found lower values for the dispersion than Holz & Linder (2005). Bergström et al. (2000) find  $\sigma_{\Delta m_{\text{lens}}} \simeq 0.04$  mag for  $z_{\text{SN}} = 1$  using simulations and assuming smooth halo profiles.

From Fig. 7, we find  $B \simeq 0.055^{+0.039}_{-0.041}$  mag. At the 95 per cent confidence level, we find  $B \lesssim 0.12$  mag. The results are thus consistent with the simulations of Holz & Linder (2005) and Bergström et al. (2000) at the 68.3 per cent confidence level.

The value of the gravitational lensing dispersion is very sensitive to the high magnification tail. For small samples of SNe Ia, which fail to sample the high magnification tail, we might therefore find

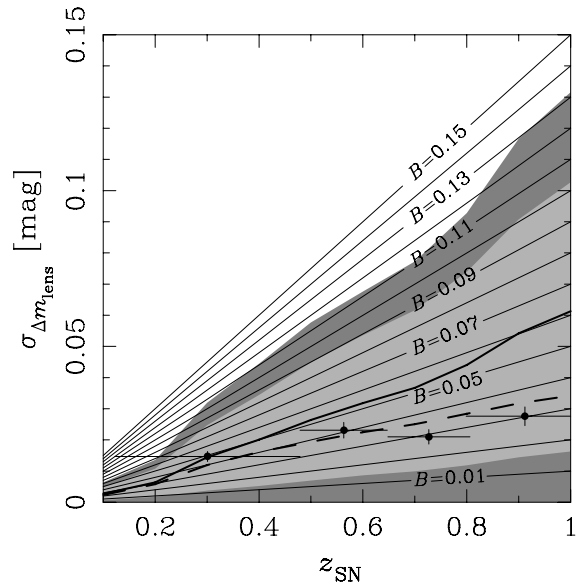


**Figure 7.** Gravitational lensing scatter as a function of redshift. The thick solid curve shows the dispersion for the best-fitting model found in Section 4.3. Light and dark shaded regions correspond to 68.3 and 95 per cent confidence level, respectively. Predictions for a simple model of the lensing scatter,  $\sigma_{\Delta m_{\text{lens}}} = B z_{\text{SN}}$ , for  $B = 0.01, 0.02, \dots, 0.15$  mag are indicated by the thin lines. The circles show the scatter in the magnification computed in four redshift bins for the sample of SNe Ia used in the analysis. Horizontal error bars indicate the width of the redshift bins. The thick dashed curve shows the dispersion for the best-fitting model when SNe Ia with  $\Delta m_{\text{SN}} < -0.25$  mag have been discarded.

a smaller dispersion. This appears to be the case for our sample of 175 SNe Ia. The circles in Fig. 7 show the lensing scatter of these SNe Ia computed for four redshift bins with  $\simeq 44$  objects in each bin. The circles are consistent with  $B \simeq 0.035$  mag, which is smaller than the value predicted by the best-fitting model. Rejecting simulated SNe Ia with  $\Delta m_{\text{lens}} < -0.25$  mag leads to the dispersion shown by the thick dashed curve, which agrees with the scatter for the SN Ia sample. Only 0.3 (0.7) per cent of the SNe Ia would be brighter than  $-0.25$  mag for SNe with redshift 0.7 (1.0). For the whole sample of 243 SNe Ia, the best-fitting model predicts the number of supernovae brighter than  $-0.25$  mag to be 0.8. For the subsample of SNe Ia used in the lensing analysis, the corresponding number is 0.6. Since the number of SNe Ia belonging to the tail is expected to be very small, our sample of SNe Ia is probably not sampling the high-redshift tail brighter than  $\Delta m_{\text{lens}} \simeq -0.25$  mag.

## 7 DISCUSSION AND SUMMARY

We have used presumably lensed SNe Ia from 3-yr of the SNLS to investigate properties of dark matter haloes of galaxies in the deep CFHTLS fields. The dark matter haloes were modelled as truncated SISs with velocity dispersion and truncation radius given by luminosity-dependent scaling laws.

Another way to probe dark matter haloes is via galaxy–galaxy lensing (Tyson et al. 1984; Brainerd, Blandford & Smail 1996; Hudson et al. 1998; Fischer et al. 2000; McKay et al. 2001; Guzik & Seljak 2002; Hoekstra et al. 2003; Hoekstra, Yee & Gladders 2004; Kleinheinrich et al. 2006; Mandelbaum et al. 2006; Parker et al. 2007; Mandelbaum, Uros & Hirata 2008; Mandelbaum et al. 2009), which relies upon measurement of shear via the ellipticity of lensed galaxies rather than the convergence. In the galaxy–galaxy



lensing literature, different truncation radius scaling laws of the form expressed by equation (15) have been explored. Hoekstra et al. (2003) considered, for example, the size of galaxy haloes either to be the same for all galaxies ( $\gamma = 0$ ) or to scale as  $\sigma^2$  ( $\gamma = 2$ ). Since the virial radius of an SIS is proportional to its velocity dispersion, another plausible scaling law would be  $\gamma = 1$ .

Fixing the exponent of the velocity dispersion scaling law, equation (13), to  $\eta = 1/3$ , we tried to constrain the truncation radius scaling law, but the data did not allow us to constrain  $r_*$  or  $\gamma$ .

We have also explored the velocity dispersion scaling law by setting  $\gamma = 0$ . Fig. 3 shows the result of this exercise. Hoekstra et al. (2004) used galaxy–galaxy lensing to investigate the properties of dark matter. They used a model slightly different from ours, namely the truncated isothermal sphere model (Brainerd et al. 1996), which has a parameter  $s$  describing the truncation scale of the halo. For a value of  $\eta$  fixed to 0.3, they found  $\sigma_* = 136 \pm 5 \pm 3 \text{ km s}^{-1}$  (statistical and systematic uncertainties) and  $s = 185_{-28}^{+30} h^{-1} \text{ kpc}$ . Parker et al. (2007) found a similar value of the velocity dispersion,  $\sigma_* = 137 \pm 11 \text{ km s}^{-1}$ , using CFHTLS data.

In another galaxy–galaxy lensing study, Kleinheinrich et al. (2006) found  $\sigma_* = 132_{-24}^{+18} \text{ km s}^{-1}$  and  $\eta = 0.37 \pm 0.15$  for SIS haloes truncated at  $350 h^{-1} \text{ kpc}$ . Our results for the velocity dispersion scaling law are in good agreement with the findings of these studies. The data prefer, however, a much smaller truncation radius.

Moreover, we tried to disentangle the scaling laws of passive and star-forming galaxies. Again we restricted ourselves to models with  $\gamma = 0$ . Passive and star-forming galaxies were assumed to obey F–J and T–F relations, respectively. The best-fitting values of the velocity dispersion and confidence level contours obtained after marginalization over  $r_*$  are shown in Fig. 6. The point  $\sigma_*^p = \sigma_*^{\text{sf}} = 0$  in this plot, which corresponds to no lensing, is excluded at the 91.6 per cent confidence level.

The results agree well with empirical F–J and T–F relations. Mitchell et al. (2005) measured the F–J relation in the  $r$  band using Sloan Digital Sky Survey data. Their measurement corresponds to a velocity dispersion normalization of  $190 \text{ km s}^{-1}$  for our choice of  $L_*$ , i.e.  $M_B = -20.3 \text{ mag}$  in the Vega system. Böhm et al. (2004) derived a redshift-dependent T–F relation using data from Pierce & Tully (1992). For a galaxy at  $z = 0$ , their findings corresponds to a normalization of  $122 \text{ km s}^{-1}$ .

Assuming the truncation radius to be given by the virial radius, we found  $\sigma_*^p < 195$  and  $\sigma_*^{\text{sf}} < 117 \text{ km s}^{-1}$ , a result which is marginally consistent with haloes truncated at the virial radius with velocity dispersion given by F–J and T–F relations. Correcting the SNe Ia for dust extinction using the results of Ménard et al. (2009a) and Ménard et al. (2009b) have no significant impact on  $\sigma_*^p$  and  $\sigma_*^{\text{sf}}$ .

Furthermore, we have used the best-fitting model with different scaling laws for passive and star-forming galaxies to investigate the gravitational lensing scatter. For a model where the scatter is proportional to source redshift,  $\sigma_{\Delta m_{\text{lens}}} = B z_{\text{SN}}$ , we find  $B \simeq 0.055_{-0.041}^{+0.039} \text{ mag}$  (at 68.3 per cent confidence level and  $B \lesssim 0.12 \text{ mag}$  at the 95 per cent confidence level). The scatter is consistent with the prediction of Holz & Linder (2005,  $B = 0.088 \text{ mag}$ ) at the 68.3 per cent confidence level.

If the best-fitting model gives an accurate description of the gravitational lensing of SNe Ia, the contribution from gravitational lensing scatter to the intrinsic dispersion ( $\simeq 0.09 \text{ mag}$ ) of the SNLS SNe Ia is very small. For SN Ia data sets with  $z_{\text{SN}} \gtrsim 1.6$ , gravitational lensing could, according to the best-fitting model, contribute significantly to the brightness scatter. The farthest known SN Ia (1997ff) with  $z_{\text{SN}} \simeq 1.8$  is indeed believed to be magnified by a few tenths of a magnitude (Lewis & Ibata 2001; Mörtzell, Gunnarsson

& Goobar 2001; Riess et al. 2001; Benítez et al. 2002; Jönsson et al. 2006).

## ACKNOWLEDGMENTS

JJ would like to thank Taia Kronborg, Julien Guy, Pierre Astier, Edvard Mörtzell and Ariel Goobar for helpful discussions. MS acknowledges support from the Royal Society.

Based on observations obtained with MegaPrime/ MegaCam, a joint project of CFHT and CEA/DAPNIA, at the Canada–France–Hawaii Telescope (CFHT) which is operated by the National Research Council (NRC) of Canada, the Institut National des Science de l’Univers of the Centre National de la Recherche Scientifique (CNRS) of France and the University of Hawaii. This work is based in part on data products produced the Canadian Astronomy Data Centre as part of the Canada–France–Hawaii Telescope Legacy Survey, a collaborative project of NRC and CNRS.

Based on observations obtained at the Gemini Observatory, which is operated by the Association of Universities for Research in Astronomy, Inc., under a cooperative agreement with the NSF on behalf of the Gemini partnership: the National Science Foundation (United States), the Science and Technology Facilities Council (United Kingdom), the National Research Council (Canada), CONICYT (Chile), the Australian Research Council (Australia), Ministério da Ciência e Tecnologia (Brazil) and Ministerio de Ciencia, Tecnología e Innovación Productiva (Argentina).

The programmes under which data were obtained at the Gemini Observatory are: GS-2003B-Q-8, GN-2003B-Q-9, GS-2004A-Q-11, GN-2004A-Q-19, GS-2004B-Q-31, GN-2004B-Q-16, GS-2005A-Q-11, GN-2005A-Q-11, GS-2005B-Q-6, GN-2005B-Q-7, GN-2006A-Q-7 and GN-2006B-Q-10.

Based in part on observations made with ESO Telescopes at the Paranal Observatory under programme IDs 171.A-0486 and 176.A-0589.

Some of the data presented herein were obtained at the W.M. Keck Observatory, which is operated as a scientific partnership among the California Institute of Technology, the University of California and the National Aeronautics and Space Administration. The Observatory was made possible by the generous financial support of the W.M. Keck Foundation.

## REFERENCES

- Astier P. et al., 2006, *A&A*, 447, 31
- Balland C. et al., 2009, *A&A*, 507, 85
- Benítez N., Riess A., Nugent P., Dickinson M., Chornock R., Filippenko A., 2002, *ApJ*, 577, L1
- Bergström L., Goliath M., Goobar A., Mörtzell E., 2000, *A&A*, 358, 13
- Bertin E., Arnouts S., 1996, *A&AS* 117, 393
- Böhm A. et al., 2004, *A&A*, 420, 97
- Boulade O. et al., 2003, *Proc. SPIE*, 4841, 72
- Brainerd T. G., Blandford R. D., Smail I., 1996, *ApJ*, 466, 623
- Bronder T. J. et al., 2008, *A&A*, 477, 717
- Bryan G., Norman M., 1998, *ApJ*, 495, 80
- Cardelli J. A., Clayton G. C., Mathis J. S., 1989, *ApJ*, 345, 245
- Conley A. et al., 2008, *ApJ*, 681, 482
- Dodelson S., Vallinotto A., 2006, *Phys. Rev. D*, 74, 063515
- Faber S. M., Jackson R. E., 1976, *ApJ*, 204, 668
- Fioc M., Rocca-Volmerange B., 1997, *A&A* 326, 950
- Fischer P. et al., 2000, *AJ*, 120, 1198
- Frieman J., 1997, *Communications Astrophys.*, 18, 323
- Gunnarsson C., Dahlén T., Goobar A., Jönsson J., Mörtzell E., 2006, *ApJ*, 640, 471
- Guy J. et al., 2007, *A&A*, 466, 11

- Guzik J., Seljak U., 2002, *MNRAS*, 355, 311
- Hoekstra H., Franx M., Kuijken K., Carlberg R. G., Yee H. K. C., 2003, *MNRAS*, 340, 609
- Hoekstra H., Yee H. K. C., Gladders M. D., 2004, *ApJ*, 606, 67
- Holz D. E., Linder E. V., 2005, *ApJ*, 631, 678
- Holz D. E., Wald R. M., 1998, *Phys. Rev. D*, 58, 063501
- Howell D. A. et al., 2005, *ApJ*, 634, 1190
- Hudson M. J., Gwyn S. D. J., Dahle H., Kaiser N., 1998, *ApJ*, 503, 531
- Ilbert O. et al., 2006, *A&A*, 457, 841
- Jönsson J., Dahlén T., Goobar A., Gunnarsson C., Mörtzell E., Lee K., 2006, *ApJ*, 639, 991
- Jönsson J., Dahlén T., Goobar A., Mörtzell E., Riess A., 2007, *J. Cosmology Astropart. Phys.*, 06, 002
- Jönsson J., Kronborg T., Mörtzell E., Sollerman J., 2008, *A&A*, 487, 467
- Jönsson J., Dahlén T., Hook I., Goobar A., Mörtzell E., 2010, *MNRAS*, 402, 526
- Jönsson J., Mörtzell E., Sollerman J., 2009, *A&A*, 493, 331
- Kantowski R., Vaughan T., Branch D., 1995, *ApJ*, 447, 35
- Kleinheinrich M. et al., 2006, *A&A*, 455, 441
- Kronborg T., et al., 2010, preprint (arXiv:1002.1249)
- Le Borgne D., Rocca-Volmerange B., 2002, *A&A*, 386, 446
- Lewis G., Ibata R., 2001, *MNRAS*, 324, L25
- Mandelbaum R., Seljak U., Kauffmann G., Hirata C. M., Brinkmann J., 2006, *MNRAS*, 368, 715
- Mandelbaum R., Seljak U., Hirata C. M., 2008, *J. Cosmology Astropart. Phys.*, 08, 006
- Mandelbaum R., Li C., Kauffmann G., White S. D. M., 2009, *MNRAS*, 393, 377
- McKay T. A. et al., 2001, preprint (astro-ph/0108013)
- Ménard B., Scranton R., Fukugita M., Richards G., 2009a, preprint (arXiv:0902.4240)
- Ménard B., Kilbinger M., Scranton R., 2009b, preprint (arXiv:0903.4199)
- Metcalf R. B., 1998, in Banday A., Sheth R., da Costa L., eds, *Evolution of Large-Scale Structure: From Recombination to Garching*, preprint (astro-ph/9810440)
- Metcalf R. B., 1999, *MNRAS*, 305, 746
- Metcalf R. B., Silk J., 1999, *ApJ*, 519, L1
- Metcalf R. B., Silk J., 2007, *Phys. Rev. Lett.*, 98, 071302
- Minty E. M., Heavens A. F., Hawkins M. R. S., 2002, *MNRAS*, 330, 378
- Mitchell J., Keeton C., Frieman J., Sheth R., 2005, *ApJ*, 622, 81
- Mörtzell E., Goobar A., Bergström L., 2001, *ApJ*, 559, 53
- Mörtzell E., Gunnarsson C., Goobar A., 2001, *ApJ*, 561, 106
- Parker L. C., Hoekstra H., Hudson M. J., van Waerbeke L., Mellier Y., 2007, *ApJ*, 669, 21
- Pierce M. J., Tully R. B., 1992, *ApJ*, 387, 47
- Rauch K. P., 1991, *ApJ*, 374, 83
- Rieke G. H., Lebofsky M. J., 1985, *ApJ*, 288, 618
- Riess A. et al., 2001, *ApJ*, 560, 49
- Sarkar D., Amblard A., Holz D. E., Cooray A., 2008, *ApJ*, 678, 1
- Savage B. D., Mathis J. S., 1979, *ARA&A*, 17, 73
- Schneider P., Ehlers J., Falco E. E., 1992, *Gravitational Lenses*. Springer-Verlag, Berlin
- Scranton R. et al., 2005, *ApJ*, 633, 589
- Seaton M. J., 1979, *MNRAS*, 187, 73
- Seljak U., Holz D. E., 1999, *A&A*, 351, L10
- Sullivan M. et al., 2006, *ApJ*, 648, 868
- Tripp R., 1998, *A&A*, 331, 815
- Tully R. B., Fisher J. R., 1977, *A&A*, 54, 661
- Tyson J. A., Valdes F., Jarvis J. F., Mills A. P. Jr, 1984, *ApJ*, 281, L59
- Wambsganss J., Cen R., Xu G., Ostriker J. P., 1997, *ApJ*, 475, L81
- Zentner A. R., Bhattacharya S., 2009, *ApJ*, 693, 1543

This paper has been typeset from a  $\text{\LaTeX}$  file prepared by the author.